Received: Added at production | Revised: Added at production | Accepted: Added at production

DOI: xxx/xxxx

RESEARCH ARTICLE

A time-based arc-length like method to remove step size effects during fracture propagation

Tim Hageman | René de Borst *

Department of Civil and Structural Engineering, University of Sheffield, Sheffield, UK

Correspondence
*René de Borst, Department of Civil and Structural Engineering, University of Sheffield, Sheffield S1 3JD, UK. Email: r.deborst@sheffield.ac.uk

Funding information
Horizon 2020 European Research Council Grant 664734 "PoroFrac"

Summary

An arc-length like method is presented which alters the size of the time increment when simulating crack propagation problems. By allowing the time increment to change during the time step a constraint can be imposed, which is used to enforce the fracture to propagate a single element length per time step. This removes the effect of the (interface) element size on propagating fractures, and therefore allows smooth fracture propagation during the simulation. The benefits of the scheme are demonstrated for three cases: mode-I crack propagation in a double cantilever beam, a shear fracture including inertial and visco-plastic effects in the surrounding material, and a pressurised fracture inside a poroelastic material. These cases highlight the ability of this scheme to obtain more accurate and non-oscillatory results for the force-displacement relation, to remove numerically-induced stepwise fracture propagation, and to allow for arbitrary propagation velocities. An added benefit is that plastic strains surrounding a fracture are no longer affected by the (interface) element size.

KEYWORDS:
Fracture propagation, adaptive time step, arc-length method, plasticity, discontinuity

1 | INTRODUCTION

Fracture propagation is a mostly unwanted, but common phenomenon in many engineering problems. The fractures can be represented using a smeared approach, for instance using gradient damage or phase-field formulations [1,2,3,4], or as a sharp discontinuity using e.g., interface elements [5,6,7], the extended finite element method [8,9,10,11], or isogeometric analysis [12,13]. While the latter class of (discrete) methods allows for a unambiguous definition of the fracture path and the corresponding fracture aperture, they limit the fracture to propagate over discrete number of element only, thus limiting the propagation of a crack to discrete interval lengths. As a result, oscillations are often observed in load-displacement curves when small load steps are used due to the simulations alternating between no fracture propagation and a sudden propagation over one or more element lengths [14,15]. Similar issues arise for time-dependent problems in which using smaller time steps results in jumps and pauses in the fracture propagation [16,17].

These issues are the result of prescribing a constant load or time increment. For time-independent cases, the load increment can be altered during the step by using an arc-length method [18,19,20,21], which allows a constraint to be enforced. This constraint was originally taken in the form of a relation between the displacements and applied force, and allows the simulation of structural behaviour such as snap-backs and snap-throughs. More recently it has been shown that energy-based constraints can be more effective [22,23].

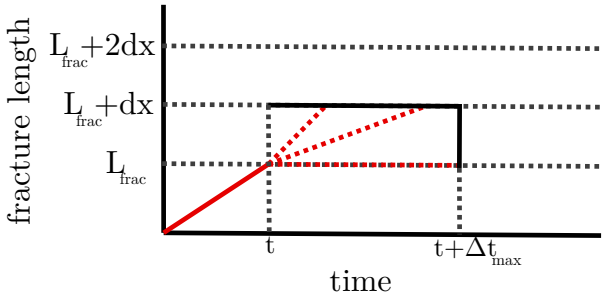

FIGURE 1 Allowable propagation window

While attempts have been made to alter the time increment as part of the finite element scheme[24,25,26], the time step size in time-dependent problems is usually prescribed at the start of a time step and kept constant. This is commonly done in explicit dynamics, where stability criteria are evaluated to allow for the largest stable time increment[27,28,29]. These criteria, however, are solely evaluated based on results from the previous steps, and therefore are unable to adapt the time step such that it would result in a continuous fracture propagation. Alternatively, the time increment can be recalculated based on converged results, allowing for additional criteria to be imposed on the fracture propagation[30,31].

Herein we will present an arc-length scheme which uses the time step similar to a load increment. In this way an arc-length like scheme can be applied to cases in which the deformations are governed by the dynamics of the system and not by changes in the external forces. The scheme will be applied to several fracture propagation problems, using the stresses ahead of the fracture as a criterion that should be fulfilled. As a result, the time increment is dynamically adapted during the current time step to allow for a continuous fracture propagation. The general scheme will be described in Section 2. Afterwards, the scheme will be elaborated and assessed for three cases: Mode-I fracture in a double cantilever beam with a time dependent load (Section 3), a shear fracture limited by inertial effects (Section 4), and a pressurised fracture propagating through a saturated poroelastic material (Section 5).

2 | TIME-BASED ARC-LENGTH LIKE METHOD

The element size effects mentioned in the Introduction are the result of interface elements being inserted along the complete boundary between two adjacent elements. Inserting new interface elements can therefore only increment the fracture length by (a multiple of) the element size. As a result, the fracture propagation during a time step is limited to propagating through a discrete number of elements. When small time or load steps are used, this results in a stepwise propagation pattern in which the fracture propagates for a single element length, and then pauses for several time steps until the propagation criterion is fulfilled and the next element fractures. When larger steps are used, small oscillations are often observed due to the simulation alternating between one and two elements fracturing during a time step.

To prevent these interface element size effects, a single element should fracture during each time step. We define the fracture propagation criterion f_c such that the fracture propagates when $f_c \geq 0$. By altering the time step size in such a manner that this criterion is exactly fulfilled at the end of the step, it is guaranteed that exactly a single element fractures during each step. This corresponds to searching for a converged solution in the region indicated in Figure 1.

This approach bears similarities to an arc-length scheme. But where in traditional arc-length methods a constraint is used in the load-displacement space, we impose a constraint in the fracture length-time space. As a result, the time increment takes the role served by of the load increment in traditional arc-length methods. However, where the load increment is allowed to be negative in order to resolve unloading and snap-back behaviour, the time increment can only be positive and, depending on the temporal discretisation scheme, non-zero.

It was chosen to use the time at the end of the current step, t^{j+1}, as an independent degree of freedom instead of the time increment. This time is treated in a similar manner as traditional degrees of freedom, and thus gets transferred from the current step to the next step, automatically keeping track of the time. Both the new time t^{j+1} and the old time t^j are available, allowing for the time increment to be determined easily. If the time increment had been taken as an independent degree of freedom instead, it would have needed to be added separately in order to keep track of the current time.

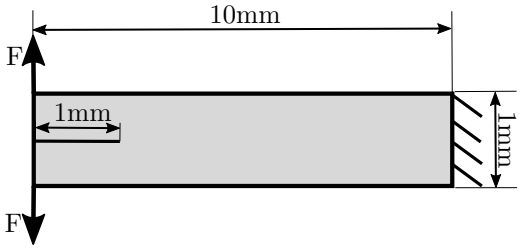

FIGURE 2 Geometry and boundary conditions for the double cantilever beam.

The fracture propagation constraint that should be fulfilled at t^{j+1} is described through:

$$f_c^* = \begin{cases} f_c^{j+1} = 0 & \text{unless} \\ t^{j+1} - t^j - \Delta t_{min} = 0 & \text{if } f_c^{j+1}(t^j + \Delta t_{min}) > 0 \\ t^{j+1} - t^j - \Delta t_{max} = 0 & \text{if } f_c^{j+1}(t^j + \Delta t_{max}) < 0 \end{cases} \tag{1}$$

in which the minimum time step size $\Delta t_{min} > 0$ is added to prevent issues due to the common singularity in time-discretisation schemes at $\Delta t = 0$ s. However, this value can be chosen sufficiently small to approximate a sudden propagating fracture, and thus allows multiple propagation steps within a short time interval. The maximum time step size Δt_{max} accounts for the possibility that the fracture does not propagate within a reasonable time, allowing for the fracture propagation to pause when a physical cause is present, e.g., due to crack arrest. This maximum time step size also warrants numerical stability of the solution scheme, forcing the solver towards the correct solution. By including these two boundaries on the time step in the used criterion, these edge cases of zero and unrealistically large time steps are caught and prevented through imposing the time increment directly in the formulation. It should be noted, however, that this usually is not needed, with the fracture propagating a single element within the allowed time increment window.

Varying the time at which the internal forces are evaluated results in a nonlinear system of equations for all but the simplest cases. To resolve these equations, an iterative Newton-Raphson scheme is employed which, in addition to the traditional degrees of freedom, includes the time at the end of the time step as a degree of freedom. This scheme is summarised as:

$$\begin{bmatrix} \frac{\partial \boldsymbol{f}_{int}}{\partial \boldsymbol{u}} & \frac{\partial \boldsymbol{f}_{int}}{\partial t} \\ \frac{\partial f_c^*}{\partial \boldsymbol{u}} & \frac{\partial f_c^*}{\partial t} + \kappa \end{bmatrix} \begin{bmatrix} \mathrm{d}\boldsymbol{u}^{j+1} \\ \mathrm{d}t^{j+1} \end{bmatrix}_{i+1} = \begin{bmatrix} \boldsymbol{f}_{ext} \\ 0 \end{bmatrix} - \begin{bmatrix} \boldsymbol{f}_{int} \\ f_c^* \end{bmatrix}_i \tag{2}$$

Dependent on the used propagation criterion, the $\partial f_c^*/\partial t$ term can be zero and the $\partial f_c^*/\partial \boldsymbol{u}$ term can be extremely sparse, resulting in a poorly conditioned or near-singular system matrix. To resolve this, a constant $\kappa \geq 0$ is added to the diagonal to improve the condition number of the system matrix. Since this term is only added to the system matrix, it does not affect the solution. It does, however, provide some damping to the changes in time obtained from the Newton-Raphson scheme, providing added stability to the scheme while possibly reducing the convergence rate.

In the remainder of this paper this scheme will be applied to three cases, demonstrating its capabilities and showcasing the advantages compared to using a constant time step. For the reference solutions which use a constant time step size, a constraint is placed on the t^{j+1} degree of freedom in a similar manner as traditional degrees of freedom, limiting the new time such that $t^{j+1} = t^j + \Delta t$. The spatial discretisation for these cases will be performed using Bézier extracted T-splines [7,13,32,33,34], exploiting their improved inter-element continuity to evaluate the stresses ahead of the fracture on the element boundaries. Since the stresses are directly evaluated ahead of the fracture tip, no interpolation functions are used inside the fracture propagation criterion. However, if standard Lagrangian elements are employed the propagation criterion can be adapted to include the interpolation used to obtain the stresses. Similar propagation criteria can also be employed for X-FEM [8,9,11] or X-IGA [15] to adapt the method to fractures propagating in arbitrary directions.

3 | CASE 1: DOUBLE CANTILEVER BEAM

The first case which we consider is the double cantilever beam. The dimensions and material properties are as in Fathi et al. [15]. The example consists of a 10 mm × 1 mm domain, through which a fracture propagates with an initial length of 1 mm as shown in Figure 2. The material is characterised by a Young's modulus $E = 100$ MPa and a Poisson ratio $\nu = 0.3$.

For this quasi-static case the equilibrium condition holds:

$$\boldsymbol{L}^T \boldsymbol{\sigma} = 0 \tag{3}$$

with $\boldsymbol{L}^T$ the divergence mapping operator. The problem is made time-dependent by imposing a constant velocity $\upsilon = 0.01\text{mm/s}$ at the tips of the beam. To obtain a clear definition for the external forces, this imposed velocity is implemented through the external forces:

$$F_{ext} = k_d(u_y \pm \upsilon\, t) \tag{4}$$

which use a dummy permeability k_d to enforce the vertical displacements u_y to be equal to the enforced displacement $\mp \upsilon t$. Finally, the fracture is propagated once σ_{yy} exceeds the tensile strength in the first integration point ahead of the fracture:

$$f_c = \sigma_{yy} - f_t \tag{5}$$

using the tensile strength $f_t = 1$ MPa. The fractured elements use an exponential traction separation law, using the fracture energy $\mathcal{G}_c = 0.1$ kN/m.

3.1 | Discretisation

The governing equations, Eq. (3) and (5), are discretised using cubic T-splines $\boldsymbol{N}$, resulting in the force vector:

$$\boldsymbol{f} = \int_\Omega \boldsymbol{B}^T \boldsymbol{D}_{el} \boldsymbol{B} \boldsymbol{u}^{j+1}\, \mathrm{d}\Omega + \int_{\Gamma_d} \boldsymbol{N}^T \tau_{czm}\, \mathrm{d}\Gamma_d - \sum_{i=1}^{2} \boldsymbol{N}^T k_d \left(\boldsymbol{N}\boldsymbol{u}^{j+1} \pm \upsilon\, t^{j+1}\right) = \boldsymbol{0} \tag{6}$$

where $\boldsymbol{B} = \boldsymbol{L}\boldsymbol{N}$, $\boldsymbol{D}_{el}$ being the linear-elastic stiffness matrix, and τ_{czm} represents the traction resulting from the traction-separation law used for fractured elements. The propagation constraint is discretised as:

$$f_c = \boldsymbol{s}_2^T \boldsymbol{D}_{el} \boldsymbol{B} \boldsymbol{u}^{j+1} - f_t = 0 \tag{7}$$

with $\boldsymbol{s}_2^T$ a vector used to select the σ_{yy} stress component. This assumes the current time step is within the allowed limits, $\Delta t_{min} < t^{j+1} - t^j < \Delta t_{max}$. When this is not the case, the limiting cases from Eq. (1) are discretised as:

$$k_t \left(t^{j+1} - t^j\right) = \begin{cases} k_t \Delta t_{min} & \text{if } t^{j+1} - t^j \leq \Delta t_{min} \\ k_t \Delta t_{max} & \text{if } t^{j+1} - t^j \geq \Delta t_{max} \end{cases} \tag{8}$$

using a sufficiently high constant k_t to enforce these time step size limits. This approach shows similarities to the dummy stiffness approach used for interface elements, where a large value is used to prevent the fracture from attaining a negative opening (or in this case, prevent negative time increments).

The discretised equations are solved using the scheme from Eq. (2), which, for the time t^{j+1} being within the limits, results in:

$$\begin{bmatrix} \int_\Omega \boldsymbol{B}^T \boldsymbol{D}_{el} \boldsymbol{B}\, \mathrm{d}\Omega + \int_{\Gamma_d} \boldsymbol{N}^T \frac{\partial \tau_{czm}^{j+1}}{\partial \boldsymbol{u}}\, \mathrm{d}\Gamma_d - \sum_{i=1}^{2} k_d \boldsymbol{N}^T \boldsymbol{N} & \mp \sum_{i=1}^{2} k_d \boldsymbol{N}^T \upsilon \\ \boldsymbol{s}_2^T \boldsymbol{D}_{el} \boldsymbol{B} & 0 \end{bmatrix} \begin{bmatrix} \mathrm{d}\boldsymbol{u}^{j+1} \\ \mathrm{d}t^{j+1} \end{bmatrix}_{i+1} = - \begin{bmatrix} \boldsymbol{f} \\ f_c \end{bmatrix}_i \tag{9}$$

Since only the traction-separation law is nonlinear, this system converges within a few iterations. For the simulations using a constant time step, the fracture propagation criterion is checked based on these converged results, and two different approaches are adapted once the fracture propagates. Either more iterations are added to re-obtain a converged solution using the new fracture length at the end of the time step, resulting in a fully implicit scheme, or the simulation continues with the next time step, resulting in a partially explicit scheme which obtains a solution using the old fracture length. For the simulations using the time-based arc-length scheme, the moment of fracture propagation coincides with the end of the time step and therefore no further iterations with the updated fracture length are performed once a converged solution is achieved.

The discretisation used 100×10 elements. To enforce the imposed external forces, a dummy stiffness $k_d = 10^{10}$ N/m is used. Since no issues arise for a zero time step size, $\Delta t_{min} = 0.0$ s is used, and the maximum time step size is chosen sufficiently large not to inhibit the results, $\Delta t_{max} = 20.0$ s.

3.2 | Results

The force-displacement results are shown in Figures 3 and 4 for the simulation using the time-based method and the simulations allowing for fracture propagation during the time step. The simulations using smaller time steps result in small oscillations due

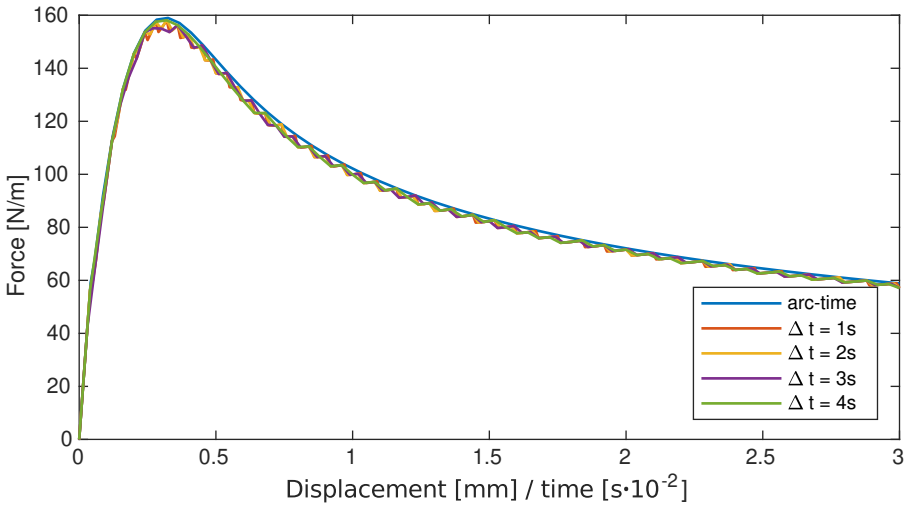

FIGURE 3 Force-displacement resulting from simulations using a constant time step, and the time-based method.

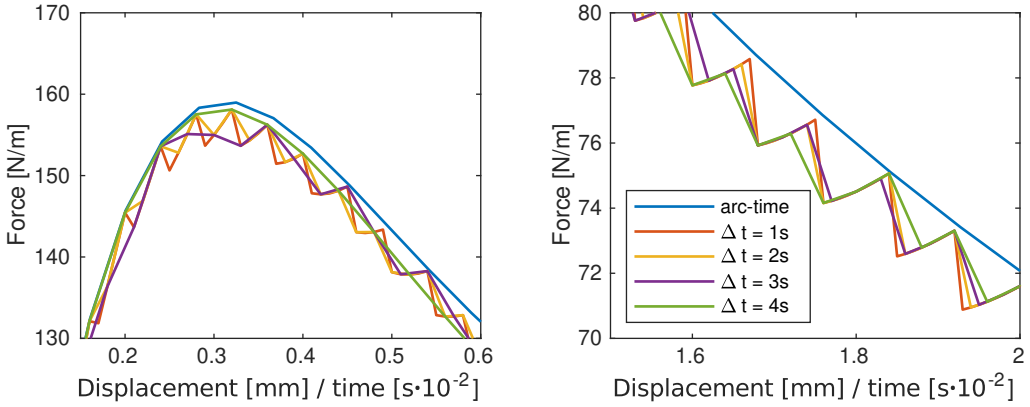

(a) Peak load **(b)** Downward slope

FIGURE 4 Force-displacement results, zoomed at areas of interest.

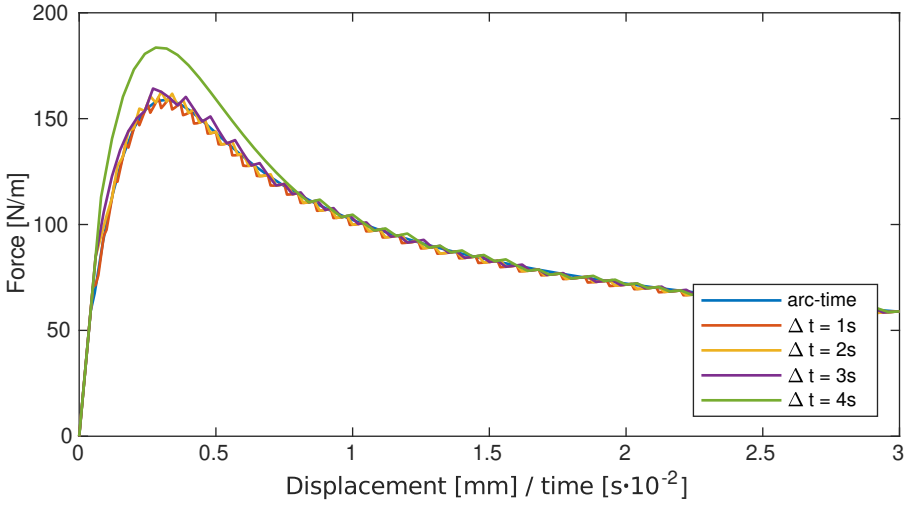

FIGURE 5 Force-displacement resulting from simulations using a constant time step while only evaluating fracture propagation at the end of the step, and the time-based method.

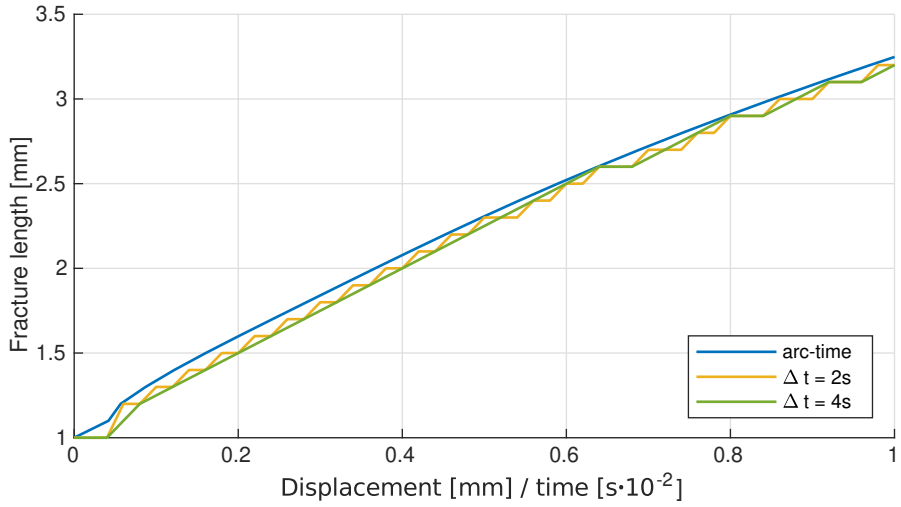

FIGURE 6 Evolution of the fracture length.

to the fracture propagating either over one element length or not at all, whereas $\Delta t = 4$ s results in a rather smooth curve near the peak load because at least one new interface element is being created during each time step. This can also be observed from the evolution of the fracture length, see Figure 6, where a continuous propagation is observed when using the largest time step up to $t = 64$ s. This figure also shows the limited propagation rates that can be obtained due to the constant time step size, with the propagation velocity corresponding to $v_{frac} = n \cdot dx/\Delta t$ with n an integer and dx the interface element size.

However, when the time step size is adapted, a smooth fracture propagation is observed throughout the entire simulation. The pauses in the fracture propagation have disappeared, and therefore no drops in the force-displacement relation are observed. Since the propagation criterion is exactly fulfilled at the end of the step, this simulation results in a higher peak load compared to the constant time step results, which consistently underestimate the load. This underestimation is a result of the fracture propagation being assumed part of the time step, thereby obtaining an external force that is insufficient to propagate the fracture another element. In contrast, by adapting the time step the peak load at the moment of fracture propagation is recorded.

Underestimating the external force can also be removed by ending the current time step at the moment the fracture propagates, as shown in Figure 5. Indeed, doing so results in the external force slightly exceeding the expected load, and stresses around the newly created fracture which exceed the propagation criterion. However, as the time step is increased, this overestimation becomes worse. With the implicit fracture propagation method two elements fractured for the first two steps of the simulation. In contrast, when the fracture propagation criterion is only checked once at the end of the simulation the stresses at the second element should already exceed the allowed stresses for two elements to fracture at once, requiring significantly higher stresses around the fracture tip, thereby limiting the propagation to a single element for the entire duration of the simulation. As a result, this simulation only converges towards the other simulations around $t = 80$ s, around the same moment the implicit propagation scheme has had two steps without fracture propagation.

4 | CASE 2: INERTIA-DRIVEN SHEAR FRACTURE

The second case which we consider is a fracture propagating due to shear stresses, while being limited by inertial and visco-plastic effects in the domain[35,36]. This case consists of a 500×250 m domain on which external forces are applied ($\tau_{xx} = 8.55$ MPa, $\tau_{yy} = 10$ MPa, $\tau_{xy} = 1.8$ MPa). To prevent stress waves from reflecting from the domain boundaries, absorbing boundary conditions are employed. An initial 75 m long fracture is present at the centre of the domain, see Figure 7, which starts to propagate due to the external stresses.

The momentum balance is given as:

$$\boldsymbol{L}^T \boldsymbol{\sigma} - \rho \ddot{\boldsymbol{u}} = 0 \tag{10}$$

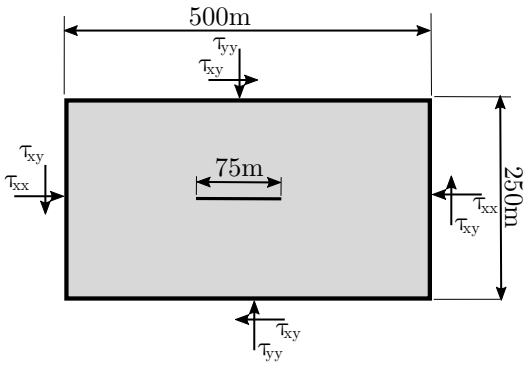

FIGURE 7 Geometry and boundary conditions for the inertia-driven fracture case

with a density $\rho = 2500$ kg/m^3. The material is assumed to exhibit visco-plastic deformations and to obey a non-associated flow rule, defined through the yield function f and the plastic potential function g:

$$f = \sqrt{3J_2} + \alpha_s p - k_s \qquad g = \sqrt{3J_2} + \beta_s p \tag{11}$$

with p the pressure and J_2 the second invariant of the deviatoric stresses. The constants are defined as $\alpha_s = 6sin(\phi)/(3 - sin(\phi))$, $\beta_s = 6sin(\psi)/(3 - sin(\psi))$, and $k_s = 6c\ cos(\phi)/(3 - sin(\phi))$, with the cohesion $c = 0$, the angle of internal friction $\phi = 31°$, and the dilatancy angle $\psi = 0°$. Up to the yield function, elastic deformations occur governed by a Young's modulus $E = 10$ GPa and a Poisson's ratio $\nu = 0.25$. Once the stress exceeds the yield function the plastic deformations are described by a linear Perzyna model:

$$\boldsymbol{\sigma} - \left(\boldsymbol{\sigma}_{trial} - \Delta\lambda \boldsymbol{D}_{el}\boldsymbol{m}_p\right) = 0 \tag{12a}$$

$$f - \frac{\eta\sigma_0}{\Delta t}\Delta\lambda = 0 \tag{12b}$$

with $\boldsymbol{m}_p$ the direction of the plastic strain, the viscosity parameter $\eta\sigma_0 = 10^7$ Pa s, and the plastic deformation increment $\Delta\lambda$. Finally, the propagation criterion for the fracture is given by:

$$f_c = \sigma_{xy} - f_p\sigma_{yy} \tag{13}$$

with $f_p = 0.45$ the peak coefficient of friction. The fractured elements use an exponential traction-separation law, also utilising this peak coefficient of friction, a residual friction coefficient $f_r = 0.045$, and a fracture release energy $\mathcal{G}_c = 17.4$ kN/m.

4.1 | Discretisation

The spatial discretisation is carried out in the same manner as in Section 3.1, using cubic T-splines. The temporal discretisation is done using a Newmark scheme, evaluating the force vectors at the new time and discretising the velocity and acceleration as:

$$\dot{\boldsymbol{u}}^{j+1} = \frac{\gamma}{\beta\left(t^{j+1} - t^j\right)}\left(\boldsymbol{u}^{j+1} - \boldsymbol{u}^j\right) - \left(\frac{\gamma}{\beta} - 1\right)\dot{\boldsymbol{u}}^j - \left(t^{j+1} - t^j\right)\left(\frac{\gamma}{2\beta} - 1\right)\ddot{\boldsymbol{u}}^j \tag{14}$$

$$\ddot{\boldsymbol{u}}^{j+1} = \frac{1}{\beta\left(t^{j+1} - t^j\right)^2}\left(\boldsymbol{u}^{j+1} - \boldsymbol{u}^j\right) - \frac{1}{\beta\left(t^{j+1} - t^j\right)}\dot{\boldsymbol{u}}^j - \left(\frac{1}{2\beta} - 1\right)\ddot{\boldsymbol{u}}^j \tag{15}$$

Using these temporal and spatial discretisations the force vector is given as:

$$\begin{aligned}\boldsymbol{f} = &\int_\Omega \boldsymbol{B}^T\boldsymbol{\sigma}^{j+1}\,\mathrm{d}\Omega + \int_\Omega \rho\boldsymbol{N}^T\boldsymbol{N}\left(\frac{1}{\beta\left(t^{j+1} - t^j\right)^2}\left(\boldsymbol{u}^{j+1} - \boldsymbol{u}^j\right) - \frac{1}{\beta\left(t^{j+1} - t^j\right)}\dot{\boldsymbol{u}}^j - \left(\frac{1}{2\beta} - 1\right)\ddot{\boldsymbol{u}}^j\right)\mathrm{d}\Omega \\ &+ \int_{\Gamma_d} \boldsymbol{N}^T\tau_{czm}\,\mathrm{d}\Gamma_d + \int_\Gamma \boldsymbol{N}^T\boldsymbol{R}^T\boldsymbol{C}\boldsymbol{R}\boldsymbol{N}\left(\frac{\gamma}{\beta\left(t^{j+1} - t^j\right)}\left(\boldsymbol{u}^{j+1} - \boldsymbol{u}^j\right) - \left(\frac{\gamma}{\beta} - 1\right)\dot{\boldsymbol{u}}^j - \left(t^{j+1} - t^j\right)\left(\frac{\gamma}{2\beta} - 1\right)\ddot{\boldsymbol{u}}^j\right)\mathrm{d}\Gamma \\ &- \int_\Gamma \boldsymbol{N}^T\boldsymbol{\tau}_{ext}\,\mathrm{d}\Gamma = \boldsymbol{0}\end{aligned} \tag{16}$$

with the rotation matrix $\boldsymbol{R}$ and the damping matrix $\boldsymbol{C} = \rho[c_s \; 0; 0 \; c_p]$, c_s and c_p being the pressure and shear wave speeds, respectively. The fracture propagation criterion from Eq. (13) is discretised as:

$$f_c = \left(\boldsymbol{s}_4^T - f_p \boldsymbol{s}_2^T\right) \boldsymbol{\sigma}^{j+1} = 0 \tag{17}$$

Equations (16) and (17) are solved using the iterative scheme from Eq. (2) as:

$$\begin{bmatrix} \boldsymbol{K}_{eff} + \boldsymbol{M} + \boldsymbol{C}^* + \int_{\Gamma_d} \boldsymbol{N}^T \frac{\partial \tau_{czm}^{j+1}}{\partial \boldsymbol{u}} \, \mathrm{d}\Gamma_d & \boldsymbol{k}_{eff} + \boldsymbol{m} + \boldsymbol{c}^* \\ \left(\boldsymbol{s}_4^T - f_p \boldsymbol{s}_2^T\right) \boldsymbol{d}_{eff}^T & 0 \end{bmatrix} \begin{bmatrix} \mathrm{d}\boldsymbol{u}^{j+1} \\ \mathrm{d}t^{j+1} \end{bmatrix}_{i+1} = - \begin{bmatrix} \boldsymbol{f} \\ f_c \end{bmatrix}_i \tag{18}$$

with the sub-matrices given by:

$$\boldsymbol{K}_{eff} = \int_\Omega \boldsymbol{B}^T \boldsymbol{D}_{eff} \boldsymbol{B} \, \mathrm{d}\Omega \tag{19a}$$

$$\boldsymbol{k}_{eff} = \int_\Omega \boldsymbol{B}^T \boldsymbol{d}_{eff} \, \mathrm{d}\Omega \tag{19b}$$

$$\boldsymbol{M} = \int_\Omega \frac{\rho}{\beta \left(t^{j+1} - t^j\right)^2} \boldsymbol{N}^T \boldsymbol{N} \, \mathrm{d}\Omega \tag{19c}$$

$$\boldsymbol{m} = \int_\Omega \rho \boldsymbol{N}^T \boldsymbol{N} \left(\frac{-2}{\beta \left(t^{j+1} - t^j\right)^3} \left(\boldsymbol{u}^{j+1} - \boldsymbol{u}^j\right) + \frac{1}{\beta \left(t^{j+1} - t^j\right)^2} \dot{\boldsymbol{u}}^j \right) \mathrm{d}\Omega \tag{19d}$$

$$\boldsymbol{C}^* = \int_\Gamma \frac{\gamma}{\beta \left(t^{j+1} - t^j\right)} \boldsymbol{N}^T \boldsymbol{R}^T \boldsymbol{C} \boldsymbol{R} \boldsymbol{N} \, \mathrm{d}\Gamma \tag{19e}$$

$$\boldsymbol{c}^* = \int_\Gamma \boldsymbol{N}^T \boldsymbol{R}^T \boldsymbol{C} \boldsymbol{R} \boldsymbol{N} \left(\frac{-\gamma}{\beta \left(t^{j+1} - t^j\right)^2} \left(\boldsymbol{u}^{j+1} - \boldsymbol{u}^j\right) - \left(\frac{\gamma}{2\beta} - 1\right) \ddot{\boldsymbol{u}}^j \right) \mathrm{d}\Gamma \tag{19f}$$

To obtain a quadratic convergence rate, the effects of plastic deformations need to be included in the effective stiffness matrix $\boldsymbol{D}_{eff}$ and the time-dependent stiffness vector $\boldsymbol{d}_{eff}$. These matrices are obtained by taking the derivatives of Eq. (12) with regards to the stresses, strains, time increment, and plastic increment, resulting in:

$$\begin{bmatrix} \boldsymbol{D}_{eff} & \boldsymbol{d}_{eff} \\ \frac{\partial \Delta\lambda}{\partial \epsilon} & \frac{\partial \Delta\lambda}{\partial t} \end{bmatrix} = \begin{bmatrix} \boldsymbol{I} + \Delta\lambda \boldsymbol{D}_{el} \frac{\partial \boldsymbol{m}_p}{\partial \boldsymbol{\sigma}} & \boldsymbol{D}_{el} \boldsymbol{m}_p \\ \frac{\partial f}{\partial \boldsymbol{\sigma}} & -\frac{\eta \sigma_0}{t^{j+1} - t^j} \end{bmatrix}^{-1} \begin{bmatrix} \boldsymbol{D}_{el} - \Delta\lambda \boldsymbol{D}_{el} \frac{\partial \boldsymbol{m}_p}{\partial \boldsymbol{\sigma}_{trial}} \boldsymbol{D}_{el} & 0 \\ 0 & -\Delta\lambda \frac{\eta \sigma_0}{\left(t^{j+1} - t^j\right)^2} \end{bmatrix} \tag{20}$$

The domain is discretised using two different meshes, using 320 ($dx = 1.56$ m) and 640 ($dx = 0.78$ m) small elements in the horizontal direction near the discontinuity and larger elements used away from the interface. Both meshes have 60 elements in the vertical direction. To enforce the initial conditions, the first $t_0 = 1$ s is done suppressing plastic deformations and not allowing the fracture to propagate. This results in the maximum allowed time step $\Delta t_{max} = 0.01$ s being used for all steps. After this initial period the fracture is allowed to propagate, resulting in a single step in which the fracture suddenly propagates with the minimum time step size $\Delta t_{min} = 10^{-5}$ s, followed by steps within the time step size limits.

4.2 | Results

A time step is considered to be converged when the normalised energy based residual becomes lower than 10^{-9}. Since a consistent stiffness matrix is used, the simulations should attain a quadratic convergence rate. However, as shown in Figure 8a, this is not the case with a sudden drop in the error at the start of the time step, followed by a super-linear (but not fully quadratic) convergence that displays oscillations. When looking at the convergence of the time step size in Figure 8b a quadratic convergence is observed, with the time error defined as $(\Delta t_j - \Delta t_{conv})/\Delta t_1$ using the "correct" time increment Δt_{conv} from the converged solution. Since the temporal degree of freedom shows a quadratic convergence rate, it is likely that the issues with the energy based residual arise due to the large variations in time step size. These large changes in time step alter the energy available during the current time step, and therefore strongly influence the energy based convergence criterion.

The evolution of the fracture length is shown in Figure 9a. While the time based arc-length scheme obtains a smooth fracture propagation, its propagation starts off much slower compared to the simulations using a constant time step. In contrast, the simulations using a constant time step show pauses between each fracture propagation for the finest time step. Using the coarser

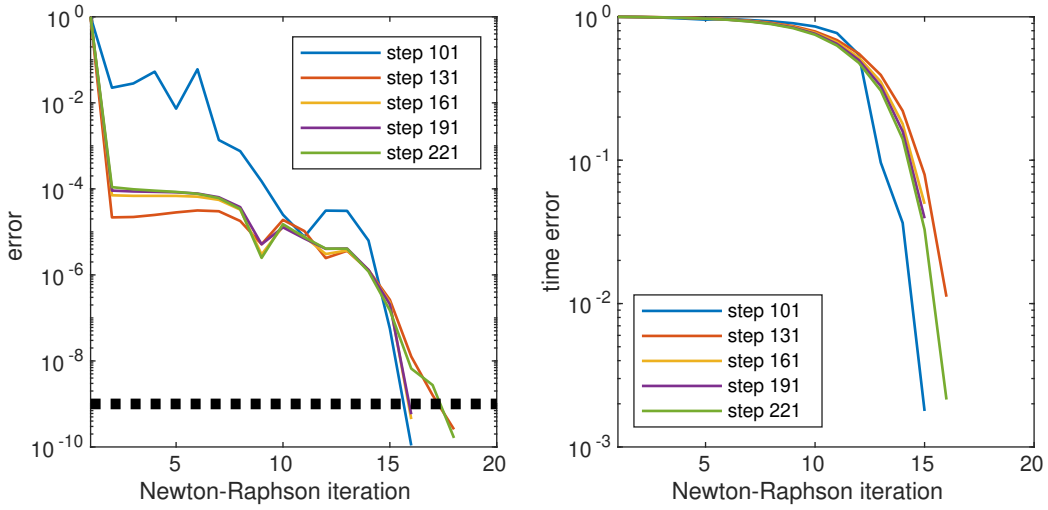

(a) Energy based convergence criterion **(b)** Single degree of freedom t^{j+1}

FIGURE 8 Convergence of the Newton-Raphson solver for selected time steps.

time step size shows pauses after 2-3 fracture propagation events, giving the impression that the simulation yields a smooth propagation with breaks, whereas this is solely the effect of the element-wise propagation.

In order to use smaller time steps for the arc-length-like scheme, a smaller element size needs to be used at the discontinuity. Results for this smaller element size are shown in Figure 9b, where the simulation with the coarse time step coincides with the results using a variable step size. This indicates that the time step size obtained using the coarse mesh was insufficient to properly capture the inertial effects and their interactions with the fracture, while the element size was sufficient using constant time steps.

The plastic deformations for the 320 horizontal element mesh are shown in Figure 10. Peaks in the plastic strain are observed for the simulations using a constant time step due to the stresses exceeding the propagation criterion around the fracture tip before the fracture propagates. While this effect is decreased for smaller time steps, it is still present. In contrast, the time based arc-length method obtains smooth plastic strains near the discontinuity, even though a coarser time step size is used compared to both other results. This difference remains upon mesh refinement, as shown in Figure 11. While the largest peaks, which correspond to the propagation pausing and restarting, have disappeared for the large time step, small peaks which correspond to stresses exceeding the propagation criterion are still present. This indicates that these effects are easily removed when using the adaptive time step method, but that very fine elements and small time steps are required when a constant time step is used.

5 | CASE 3: PRESSURISED FRACTURE INSIDE POROELASTIC MATERIAL

The final case highlights the ability of the method to simulate multi-physics problems. For this purpose we simulate a fracture filled with a pressurised fluid propagating through a poro-elastic medium[37,38,39]. The domain is 80×160 m with a fracture with initial length $L_{frac} = 0.5$ m at the left boundary with an imposed inflow $Q_{in} = 0.5\text{m}^2/\text{s}$, see Figure 12.

The stresses inside the poroelastic material are governed by the quasi-static momentum balance of the solid-fluid mixture:

$$\boldsymbol{L}^T (\boldsymbol{\sigma} - \alpha p \boldsymbol{m}) = 0 \tag{21}$$

with the stresses inside the porous solid $\boldsymbol{\sigma}$ governed by a linear-elastic model, $E = 15$ GPa and $\nu = 0.2$. The interstitial fluid pressure is denoted by p, the Biot coefficient $\alpha = 1.0$ and $\boldsymbol{m} = [1\ 1\ 0]^T$. The mass balance is used to describe the interstitial pressure changes due to the solid compression and the diffusion of the fluid:

$$\frac{1}{M}\dot{p} + \boldsymbol{\nabla} \cdot \dot{\boldsymbol{u}} - \boldsymbol{\nabla} \cdot \left(\frac{k}{\mu} \boldsymbol{\nabla} p \right) = 0 \tag{22}$$

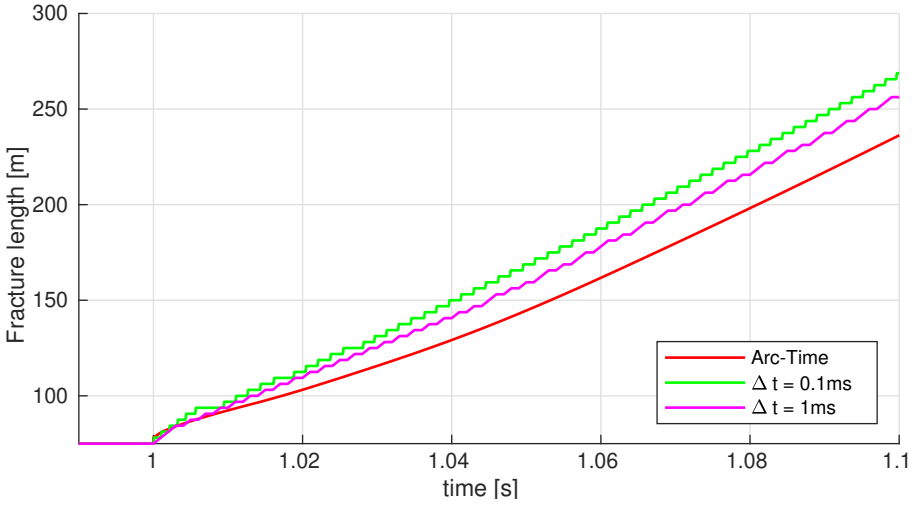

(a) 320 horizontal elements

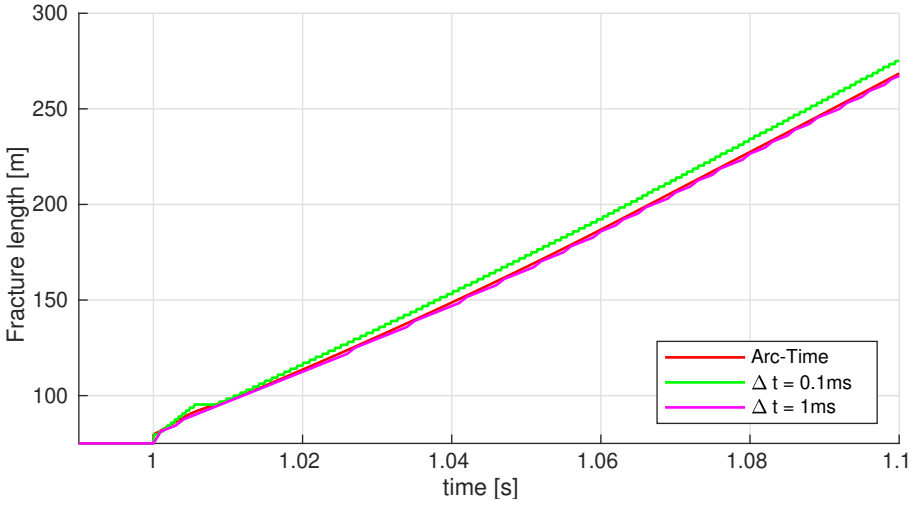

(b) 640 horizontal elements

FIGURE 9 Fracture propagation

with the Biot modulus $M = 4.41$ GPa, the intrinsic permeability $k = 10^{-14}$ m^2, and the viscosity $\mu = 10^{-3}$ Pa $\cdot$ s. The fluid flow within the fracture with opening height h is modelled using a discontinuous pressure model[16,40,41]:

$$k_i \left(2p_d - p^+ - p^-\right) - \frac{\partial}{\partial x}\left(\frac{h^3}{12\mu}\frac{\partial p_d}{\partial x}\right) + \dot{h} = 0 \tag{23}$$

allowing for a jump between the discontinuity pressure p_d and the interstitial fluid pressure by imposing an interface permeability $k_i = 10^{-10}$ m/Pa s. Finally, the fracture propagation criterion from Eq. (5) is used with $f_t = 0.1$ MPa and $\mathcal{G}_c = 0.1$ kN/m.

5.1 | Discretisation

Cubic T-splines are used for the spatial discretisation of the interstitial and discontinuity fluid pressures, $\boldsymbol{N}_p$ and $\boldsymbol{N}_d$ while quartic T-splines are used for the solid deformations, $\boldsymbol{N}_s$. The use of this unequal order mesh is common in order to fulfil the inf-sup condition[42], and thereby to prevent spurious pressure oscillations[43]. Using an implicit Euler scheme, the momentum and mass

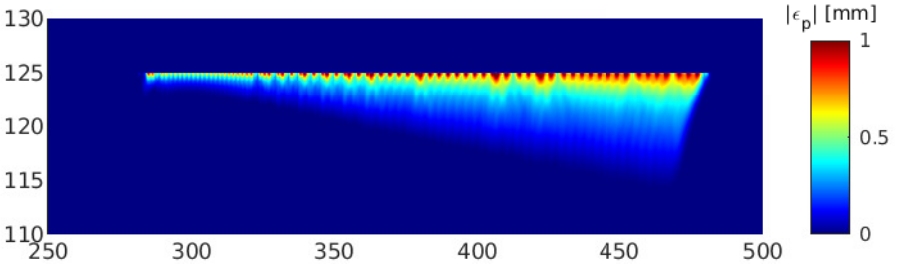

(a) $\Delta t = 1$ ms, $t = 1.2$ s

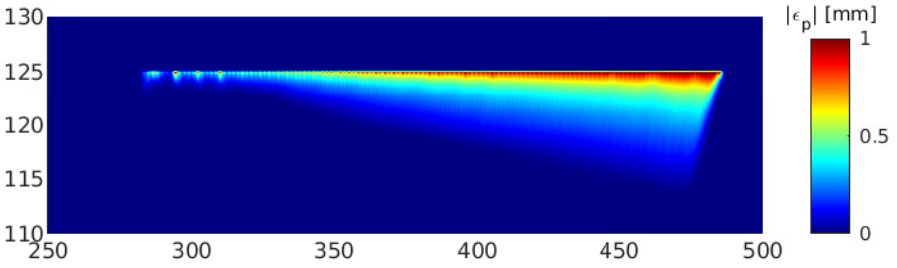

(b) $\Delta t = 0.1$ ms, $t = 1.2$ s

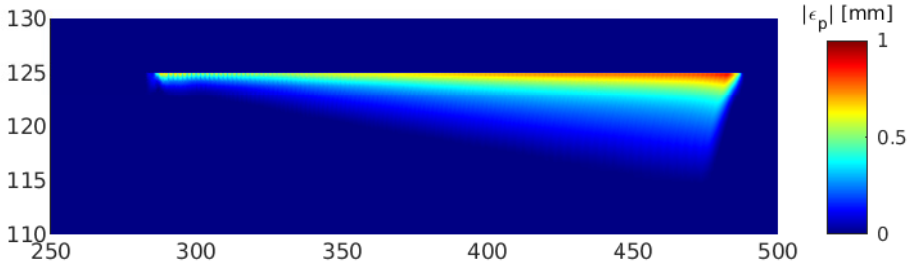

(c) Time-based propagation method, $t = 1.219$ s

FIGURE 10 Plastic strains around the right fracture tip using 320 horizontal elements.

balances are discretised as:

$$\begin{aligned} \boldsymbol{f} = &\int_{\Omega} \boldsymbol{B}_s^T \boldsymbol{D}_{el} \boldsymbol{B}_s \boldsymbol{u}^{j+1} \, \mathrm{d}\Omega - \int_{\Omega} \alpha \boldsymbol{B}_s^T \boldsymbol{m} \boldsymbol{N}_p \boldsymbol{p}^{j+1} \, \mathrm{d}\Omega + \int_{\Gamma_d} \boldsymbol{N}_s^T \tau_{czm} \, \mathrm{d}\Gamma_d \\ &+ \int_{\Gamma_d} \boldsymbol{N}_s^T \boldsymbol{n}_d \boldsymbol{N}_d \boldsymbol{p}_d^{j+1} \, \mathrm{d}\Gamma_d - \int_{\Gamma} \boldsymbol{N}_s^T \tau_{ext} \, \mathrm{d}\Gamma = \boldsymbol{0} \end{aligned} \tag{24}$$

$$\begin{aligned} \boldsymbol{q} = &\int_{\Omega} \frac{1}{M\left(t^{j+1} - t^j\right)} \boldsymbol{N}_p^T \boldsymbol{N}_p \left(\boldsymbol{p}^{j+1} - \boldsymbol{p}^j\right) \, \mathrm{d}\Omega + \int_{\Omega} \frac{\alpha}{t^{j+1} - t^j} \boldsymbol{N}_p^T \boldsymbol{m}^T \boldsymbol{B}_s \left(\boldsymbol{u}^{j+1} - \boldsymbol{u}^j\right) \, \mathrm{d}\Omega \\ &+ \int_{\Omega} \frac{k}{\mu} \boldsymbol{\nabla} \boldsymbol{N}_p^T \boldsymbol{\nabla} \boldsymbol{N}_p \boldsymbol{p}^{j+1} \, \mathrm{d}\Omega + \int_{\Gamma_d} k_i \boldsymbol{N}_p^T \left(\boldsymbol{N}_p \boldsymbol{p}^{j+1} - \boldsymbol{N}_d \boldsymbol{p}_d^{j+1}\right) \, \mathrm{d}\Gamma_d - \int_{\Gamma} \boldsymbol{N}_p^T q_{ext} \, \mathrm{d}\Gamma = \boldsymbol{0} \end{aligned} \tag{25}$$

$$\begin{aligned} \boldsymbol{q}_d = &\int_{\Gamma_d} -\frac{h^3}{12\mu} \boldsymbol{\nabla} \boldsymbol{N}_d^T \boldsymbol{\nabla} \boldsymbol{N}_d \boldsymbol{p}_d^{j+1} \, \mathrm{d}\Gamma_d - \int_{\gamma_d} \frac{1}{t^{j+1} - t^j} \boldsymbol{N}_d^T \boldsymbol{N}_s \left(\llbracket \boldsymbol{u} \rrbracket^{j+1} - \llbracket \boldsymbol{u} \rrbracket^j\right) \, \mathrm{d}\Gamma_d \\ &+ \int_{\Gamma_d} k_i \boldsymbol{N}_d^T \left(\boldsymbol{N}_p \boldsymbol{p}^{+j+1} + \boldsymbol{N}_p \boldsymbol{p}^{-j+1} - 2\boldsymbol{N}_d \boldsymbol{p}_d^{j+1}\right) \, \mathrm{d}\Gamma_d + \int_{\partial\Gamma_d} \boldsymbol{N}_d^T Q_{ext} \, \mathrm{d}\partial\Gamma_d = \boldsymbol{0} \end{aligned} \tag{26}$$

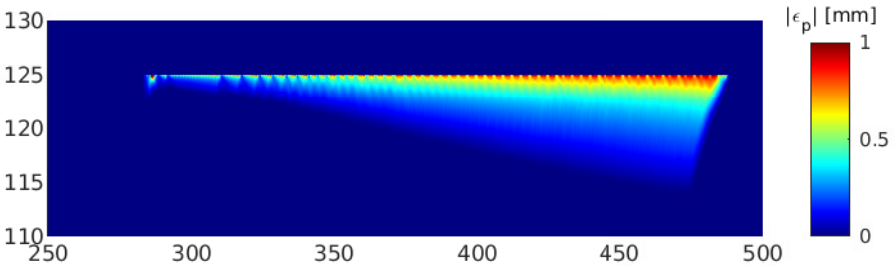

(a) $\Delta t = 1$ ms, $t = 1.2$ s

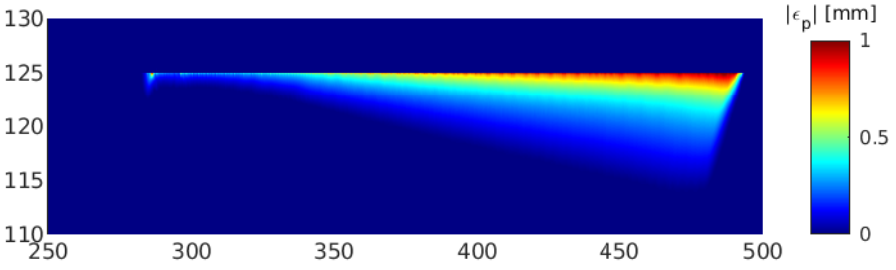

(b) $\Delta t = 0.1$ ms, $t = 1.2$ s

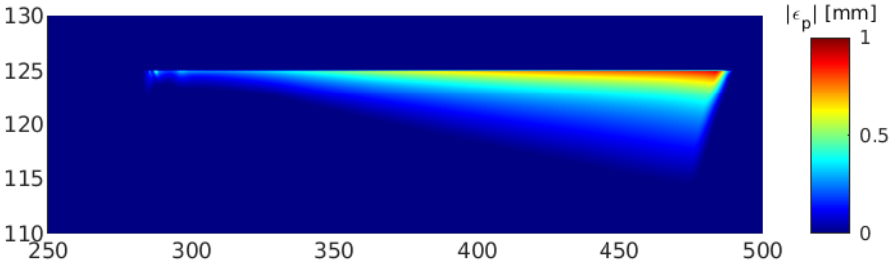

(c) Time-based propagation method, $t = 1.200$ s

FIGURE 11 Plastic strains around the right fracture tip using 640 horizontal elements.

Equations (24)-(26) and the fracture propagation criterion from Eq. (5) are solved in a monolithic manner using the scheme from Eq. (2) as:

$$\begin{bmatrix} \boldsymbol{K}+\boldsymbol{K}_d & \boldsymbol{Q}_s & \boldsymbol{Q}_d & \boldsymbol{0} \\ \boldsymbol{Q}_f & \boldsymbol{C}+\boldsymbol{H}+\boldsymbol{H}_{p,p} & \boldsymbol{H}_{p,d} & \boldsymbol{c}+\boldsymbol{q}_f \\ \boldsymbol{Q}_d+\boldsymbol{H}_d & \boldsymbol{H}_{d,p} & \boldsymbol{H}_{d,d} & \boldsymbol{q}_{dt} \\ \boldsymbol{s}_2^T\boldsymbol{D}_{el}\boldsymbol{B}_s & \boldsymbol{0} & \boldsymbol{0} & \kappa \end{bmatrix} \begin{bmatrix} \mathrm{d}\boldsymbol{u}^{j+1} \\ \mathrm{d}\boldsymbol{p}^{j+1} \\ \mathrm{d}\boldsymbol{p}_d^{j+1} \\ \mathrm{d}t^{j+1} \end{bmatrix}_{i+1} = -\begin{bmatrix} \boldsymbol{f} \\ \boldsymbol{q} \\ \boldsymbol{q}_d \\ f_c \end{bmatrix}_i \tag{27}$$

in which the constant $\kappa = 10^5$ Pa is included to improve the stability of the solver and the conditioning of the matrix. While this stabilisation decreased the convergence rate to linear, it was necessary to obtain converged solutions. The matrices used in Eq. (27) are given in the Appendix.

The results are presented for two meshes, a coarse mesh using elements with $dx = 0.5$ m near the discontinuity, and a finer mesh using $dx = 0.125$ m. Both these meshes use coarser elements away from the discontinuity. No minimum time step increment is enforced for the results presented in Figure 13, whereas $\Delta t_{min} = 0.01$ s is used for all other simulations.

5.2 | Results

The fluid flux vectors, Eq. (25)-(26), are normally multiplied by $-\Delta t$ to create a more symmetric tangential matrix. However, it was seen that this drastically impacted the convergence. An explanation for this is the singularity at $\Delta t = 0$ that is created by the $1/\Delta t$ terms providing a "resistance" against going towards a negative time step increment in the Newton-Raphson algorithm, whereas this resistance is not present if the governing equations are multiplied. As a result, the system tries to preserve a positive time step increment when the $1/\Delta t$ terms are present, pressurising the fracture and thereby propagating the fracture. When

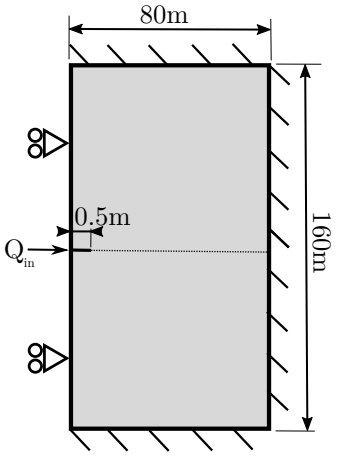

FIGURE 12 Geometry and boundary conditions used for the pressurised fracture.

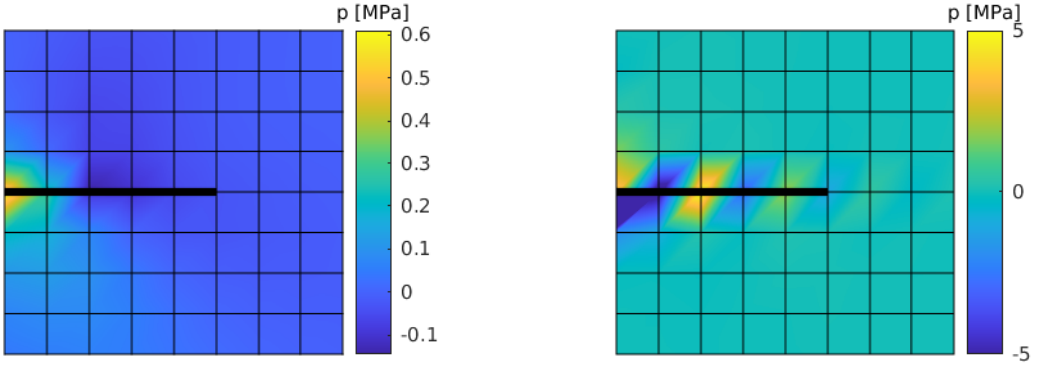

(a) Not multiplied, $t = 0.18$ s

(b) Multiplied with Δt, $t = -2.1 \cdot 10^{-5}$ s

FIGURE 13 Effect of multiplying the governing equations on the interstitial fluid pressure after the first time step without enforcing a minimum time step increment Δt_{min}

Δt terms are present, the governing equations try to converge towards a negative time step, thereby oscillating between the minimum time step limit and the fracture propagation criterion. Removing this minimum time step limit reveals the solution the system prefers to converge to, see Figure 13, namely to slightly decrease the time step such that the fluid diffusion terms cause a build-up of the pressure, with these strong pressure oscillations driving the fracture propagation.

Results with a constant time step size are presented in Figure 14. The time based arc-length scheme is able to obtain a continuous fracture propagation, whereas steps are observed when a constant time step is used. Furthermore, with the largest time step a single propagation velocity with occasional single time step pauses is obtained for the complete simulation. As was the case in the previously presented results, refining the mesh reduces the steps in the fracture propagation for small time steps, and approximates a more continuous propagation. Comparing the results for the coarse mesh with the fine mesh, shows that the coarse mesh is sufficient to accurately resolve the propagation when the arc-length-like scheme is used, whereas the finer mesh is necessary for the constant time step sizes to obtain correct results.

6 | CONCLUDING REMARKS

We have presented a time-based arc-length like scheme which adapts the time increment to allow the fracture to propagate over a single element length. In addition to the spatial degrees of freedom, the time at the end of the step is resolved using a

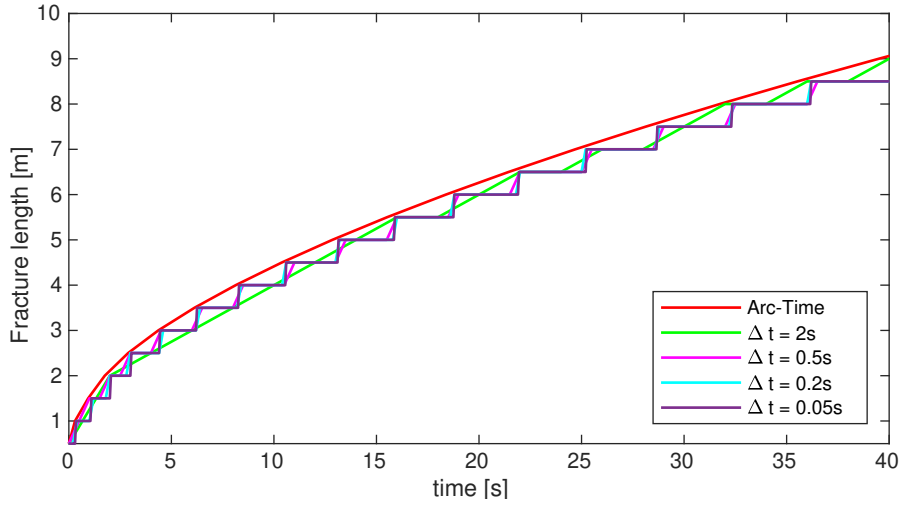

(a) $dx = 0.5$ m

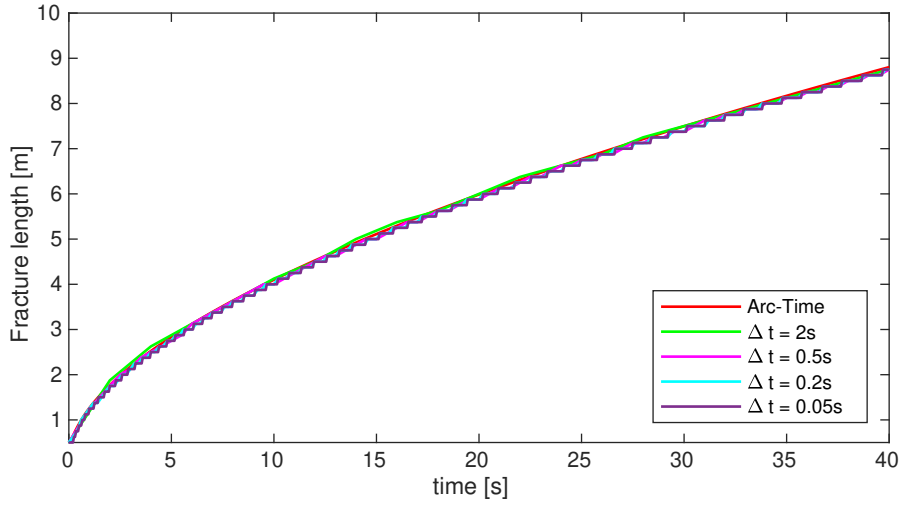

(b) $dx = 0.125$ m

FIGURE 14 Fracture propagation

single monolithic scheme. By enforcing a single element to fracture at the end of each step a continuous fracture propagation is obtained. In contrast, propagation becomes step-wise when a constant and small time increment is used, or shows pauses when larger time steps are used. We note that the physics can dictate step-wise crack propagation[44], and the present scheme helps to separate numerical effects from truly physical effects.

The advantages of the scheme have been demonstrated through three cases. The double cantilever beam showed the ability to accurately capture force-displacement behaviour without over or underestimating the peak load. This case furthermore showed the limited propagation velocities that could be obtained when using a constant time increment, whereas using a variable increment smooth propagation was obtained. The shear fracture case highlighted the benefits of a smooth fracture propagation, resulting in smoother plastic strain fields around the fracture, i.e. without effects of the (interface) element size. It also showed the ability to attain a quadratic convergence rate of the scheme. In the final case it was demonstrated showed that the same conclusions hold for poroelastic problems, which indicating some issues which can arise regarding the convergence in diffusion-dominated problems.

ACKNOWLEDGEMENT

Financial support through H2020 European Research Council Advanced Grant 664734 "PoroFrac" is gratefully acknowledged.

DATA AVAILABILITY STATEMENT

Data sharing is not applicable to this article since no data sets were generated or analysed during this study.

DECLARATION OF CONFLICT OF INTEREST

The authors declare that they have no conflict of interest and that the research findings reported here have not been published elsewhere or are under review for another publication.

The authors also declare that just before submission of this research they became aware of a similar method, submitted for peer review by G. Ren and R.M. Younis. Their manuscript *Efficient co-solution of time-step size and independent state in fluid-driven fracture propagation simulation using embedded meshes*, submitted to the International Journal for Numerical Methods in Engineering, describes a scheme which shows similarities with the method detailed in this research, but they apply it to enforce a set propagation length using XFEM, and have a more limited scope as the manuscript is confined to poroelasticity. The methods and the results described here have been obtained before the authors became aware of this manuscript, and have not been influenced in any way by this paper.

APPENDIX TANGENTIAL STIFFNESS SUB-MATRICES

The system matrices used in Eq. (27) related to the momentum balance are given by:

$$\boldsymbol{K} = \int_{\Omega} \boldsymbol{B}_s^T \boldsymbol{D}_{el} \boldsymbol{B}_s \, \mathrm{d}\Omega$$

$$\boldsymbol{K}_d = \int_{\Gamma_d} \boldsymbol{N}_s^T \frac{\boldsymbol{\tau}_{czm}}{\partial \boldsymbol{u}} \, \mathrm{d}\Gamma_d$$

$$\boldsymbol{Q}_s = \int_{\Omega} -\alpha \boldsymbol{B}_s^T \boldsymbol{m} \boldsymbol{N}_p \, \mathrm{d}\Omega$$

$$\boldsymbol{Q}_d = \int_{\Gamma_d} \boldsymbol{N}_s^T \boldsymbol{n}_d \boldsymbol{N}_d \, \mathrm{d}\Gamma_d$$

the matrices related to the mass balance of the poroelastic material as:

$$\boldsymbol{Q}_f = \int_\Omega \frac{\alpha}{t^{j+1} - t^j} \boldsymbol{N}_p^T \boldsymbol{m}^T \boldsymbol{B}_s \, \mathrm{d}\Omega$$

$$\boldsymbol{C} = \int_\Omega \frac{1}{M\left(t^{j+1} - t^j\right)} \boldsymbol{N}_p^T \boldsymbol{N}_p \, \mathrm{d}\Omega$$

$$\boldsymbol{H} = \int_\Omega \frac{k}{\mu} \boldsymbol{\nabla} \boldsymbol{N}_p^T \boldsymbol{\nabla} \boldsymbol{N}_p \, \mathrm{d}\Omega$$

$$\boldsymbol{H}_{p,p} = \int_{\Gamma_d} k_i \boldsymbol{N}_p^T \boldsymbol{N}_p \, \mathrm{d}\Gamma_d$$

$$\boldsymbol{H}_{p,d} = \int_{\Gamma_d} -k_i \boldsymbol{N}_p^T \boldsymbol{N}_d \, \mathrm{d}\Gamma_d$$

$$\boldsymbol{c} = \int_\Omega \frac{-1}{M\left(t^{j+1} - t^j\right)^2} \boldsymbol{N}_p^T \boldsymbol{N}_p \left(\boldsymbol{p}^{j+1} - \boldsymbol{p}^j\right) \, \mathrm{d}\Omega$$

$$\boldsymbol{q}_f = \int_\Omega \frac{-\alpha}{\left(t^{j+1} - t^j\right)^2} \boldsymbol{N}_p^T \boldsymbol{m}^T \boldsymbol{B}_s \left(\boldsymbol{u}^{j+1} - \boldsymbol{u}^j\right) \, \mathrm{d}\Omega$$

and the matrices related to the mass balance of the discontinuity as:

$$\boldsymbol{Q}_d = \int_{\Gamma_d} \frac{-1}{t^{j+1} - t^j} \boldsymbol{N}_d^T \boldsymbol{N}_{ds} \, \mathrm{d}\Gamma_d$$

$$\boldsymbol{H}_d = \int_{\Gamma_d} -\frac{h^2}{4\mu} \boldsymbol{\nabla} \boldsymbol{N}_d^T \boldsymbol{N}_d \boldsymbol{p}_d^{j+1} \boldsymbol{N}_{ds} \, \mathrm{d}\Gamma_d$$

$$\boldsymbol{H}_{d,p} = \int_{\Gamma_d} k_i \boldsymbol{N}_d^T \boldsymbol{N}_p \, \mathrm{d}\Gamma_d$$

$$\boldsymbol{H}_{d,d} = \int_{\Gamma_d} -2k_i \boldsymbol{N}_d^T \boldsymbol{N}_d - \frac{h^3}{12\mu} \boldsymbol{\nabla} \boldsymbol{N}_d^T \boldsymbol{\nabla} \boldsymbol{N}_d \, \mathrm{d}\Gamma_d$$

$$\boldsymbol{q}_{dt} = \int_{\Gamma_d} \frac{1}{\left(t^{j+1} - t^j\right)^2} \boldsymbol{N}_d^T \boldsymbol{N}_s \left(\llbracket \boldsymbol{u} \rrbracket^{j+1} - \llbracket \boldsymbol{u} \rrbracket^j\right) \, \mathrm{d}\Gamma_d$$

References

1. Peerlings RHJ, de Borst R, Brekelmans WAM, de Vree HPJ. Gradient-enhanced damage for quasi-brittle materials. *International Journal for Numerical Methods in Engineering* 1996; 39: 3391–3403.

2. Francfort GA, Marigo JJ. Revisiting brittle fracture as an energy minimization problem. *Journal of the Mechanics and Physics of Solids* 1998; 46: 1319–1342.

3. Bourdin B, Francfort GA, Marigo JJ. Numerical experiments in revisited brittle fracture. *Journal of the Mechanics and Physics of Solids* 2000; 48: 797–826.

4. de Borst R, Verhoosel CV. Gradient damage *vs* phase-field approaches for fracture: Similarities and differences. *Computer Methods in Applied Mechanics and Engineering* 2016; 312: 78–94.

5. Schellekens JCJ, de Borst R. On the numerical integration of interface elements. *International Journal for Numerical Methods in Engineering* 1993; 36: 43–66.

6. Allix O, Corigliano A. Geometrical and interfacial non-linearities in the analysis of delamination in composites. *International Journal of Solids and Structures* 1999; 36: 2189–2216.

7. Vignollet J, May S, de Borst R. On the numerical integration of isogeometric interface elements. *International Journal for Numerical Methods in Engineering* 2015; 102: 1733–1749

8. Belytschko T, Black T. Elastic crack growth in finite elements with minimal remeshing. *International Journal for Numerical Methods in Engineering* 1999; 45: 601–620.

9. Moës N, Dolbow J, Belytschko T. A finite element method for crack growth without remeshing. *International Journal for Numerical Methods in Engineering* 1999; 46: 131–150.

10. Remmers JJC, de Borst R, Needleman A. The simulation of dynamic crack propagation using the cohesive segments method. *Journal of the Mechanics and Physics of Solids* 2008; 56: 70–92.

11. Fries TP, Belytschko T. The extended/generalized finite element method: An overview of the method and its applications. *International Journal for Numerical Methods in Engineering* 2010; 84: 253–304.

12. Chen L, Lingen EJ, de Borst R. Adaptive hierarchical refinement of NURBS in cohesive fracture analysis. *International Journal for Numerical Methods in Engineering* 2017; 112: 2151–2173.

13. Chen L, Verhoosel CV, de Borst R. Discrete fracture analysis using locally refined T-splines. *International Journal for Numerical Methods in Engineering* 2018; 116: 117–140.

14. Moonen P, Carmeliet J, Sluys LJ. A continuous–discontinuous approach to simulate fracture processes in quasi-brittle materials. *Philosophical Magazine* 2008; 88: 3281–3298

15. Fathi F, Chen L, de Borst R. Extended isogeometric analysis for cohesive fracture. *International Journal for Numerical Methods in Engineering* 2020; 121: 4584–4613.

16. Remij EW, Remmers JJC, Huyghe JM, Smeulders DMJ. An investigation of the step-wise propagation of a mode-II fracture in a poroelastic medium. *Mechanics Research Communications* 2017; 80: 10–15

17. Pervaiz Fathima KM, de Borst R. Implications of single or multiple pressure degrees of freedom at fractures in fluid-saturated porous media. *Engineering Fracture Mechanics* 2019; 213: 1–20

18. Ramm E. Strategies for tracing the nonlinear response near limit points. In: Wunderlich W, Stein E, Bathe KJ., eds. *Nonlinear Finite Element Analysis in Structural Mechanics.* Berlin - Heidelberg: Springer-Verlag. 1981 (pp. 63–89).

19. Crisfield MA. A fast incremental/iterative solution procedure that handles "snap-through". *Computers and Structures* 1981; 13: 55–62.

20. de Borst R, Crisfield MA, Remmers JJC, Verhoosel CV. *Non-Linear Finite Element Analysis of Solids and Structures*. Chichester: John Wiley & Sons. Second ed. 2012.

21. Crisfield MA. An arc-length method including line searches and accelerations. *International Journal for Numerical Methods in Engineering* 1983; 19: 1269–1289.

22. Gutiérrez MA. Energy release control for numerical simulations of failure in quasi-brittle solids. *Communications in Numerical Methods in Engineering* 2004; 20: 19–29.

23. May S, Vignollet J, de Borst R. A new arc-length control method based on the rates of the internal and the dissipated energy. *Engineering Computations* 2016; 33: 100–115

24. van den Boogaard AH, de Borst R, van den Bogert PAJ. An adaptive time-stepping algorithm for quasistatic processes. *Communications in Numerical Methods in Engineering* 1994; 10: 837–844

25. van Zijl GPAG, de Borst R, Rots JG. A numerical model for the time-dependent cracking of cementitious materials. *International Journal for Numerical Methods in Engineering* 2001; 52: 637–654.

26. Chaimoon K, Attard MM, Tin-Loi F. Crack propagation due to time-dependent creep in quasi-brittle materials under sustained loading. *Computer Methods in Applied Mechanics and Engineering* 2008; 197: 1938–1952

27. Huang M, Yue ZQ, Tham LG, Zienkiewicz OC. On the stable finite element procedures for dynamic problems of saturated porous media. *International Journal for Numerical Methods in Engineering* 2004; 61: 1421–1450

28. Menouillard T, Réthoré J, Moës N, Combescure A, Bung H. Mass lumping strategies for X-FEM explicit dynamics: Application to crack propagation. *International Journal for Numerical Methods in Engineering* 2008; 74: 447–474

29. Almani T, Kumar K, Singh G, Wheeler MF. Stability of multirate explicit coupling of geomechanics with flow in a poroelastic medium. *Computers and Mathematics with Applications* 2019; 78: 2682–2699

30. Shauer N, Duarte CA. Improved algorithms for generalized finite element simulations of three-dimensional hydraulic fracture propagation. *International Journal for Numerical and Analytical Methods in Geomechanics* 2019; 43: 2707–2742

31. Ren G, Younis RM. An integrated numerical model for coupled poro-hydro-mechanics and fracture propagation using embedded meshes. *Computer Methods in Applied Mechanics and Engineering* 2021; 376: 113606

32. Bazilevs Y, Calo VM, Cottrell JA, et al. Isogeometric analysis using T-splines. *Computer Methods in Applied Mechanics and Engineering* 2010; 199: 229–263

33. Scott MA, Borden MJ, Verhoosel CV, Sederberg TW, Hughes TJR. Isogeometric finite element data structures based on Bézier extraction of T-splines. *International Journal for Numerical Methods in Engineering* 2011; 88: 126–156

34. Scott MA, Li X, Sederberg TW, Hughes TJR. Local refinement of analysis-suitable T-splines. *Computer Methods in Applied Mechanics and Engineering* 2012; 213-216: 206–222

35. Templeton EL, Rice JR. Off-fault plasticity and earthquake rupture dynamics: 1. Dry materials or neglect of fluid pressure changes. *Journal of Geophysical Research: Solid Earth* 2008; 113: B09306

36. Hageman T, Sabet SA, de Borst R. Convergence in non-associated plasticity and fracture propagation for standard, rate-dependent, and Cosserat continua. *International Journal for Numerical Methods in Engineering* 2021; 122: 777–795

37. Secchi S, Simoni L, Schrefler BA. Mesh adaptation and transfer schemes for discrete fracture propagation in porous materials. *International Journal for Numerical and Analytical Methods in Geomechanics* 2007; 31: 331–345

38. Ni T, Pesavento F, Zaccariotto M, Galvanetto U, Zhu QZ, Schrefler BA. Hybrid FEM and peridynamic simulation of hydraulic fracture propagation in saturated porous media. *Computer Methods in Applied Mechanics and Engineering* 2020; 366: 113101

39. Hageman T, de Borst R. A refined two-scale model for Newtonian and non-Newtonian fluids in fractured poroelastic media. *Journal of Computational Physics* 2021; 441: 110424

40. de Borst R. Fluid flow in fractured and fracturing porous media: A unified view. *Mechanics Research Communications* 2017; 80: 47–57

41. de Borst R. *Computational Methods for Fracture in Porous Media*. New York: Elsevier . 2017.

42. Chapelle D, Bathe KJ. The inf-sup test. *Computers & Structures* 1993; 47: 537–545

43. Irzal F, Remmers JJC, Verhoosel CV, de Borst R. Isogeometric finite element analysis of poroelasticity. *International Journal for Numerical and Analytical Methods in Geomechanics* 2013; 37: 1891–1907

44. Hageman T, de Borst R. Stick-slip behavior in shear fracture propagation including the effect of fluid flow. *International Journal for Numerical and Analytical Methods in Geomechanics* 2021; 45: 965–989.